Chiral spin textures of strongly interacting particles in quantum dots

Catherine J. Stevenson and Jordan Kyriakidis[*]

Department of Physics and Atmospheric Science, Dalhousie University, Halifax, Nova Scotia, Canada B3H 3J5

We probe for statistical and Coulomb-induced spin textures among the low-lying states of repulsively interacting particles confined to potentials that are both rotationally and time-reversal invariant. In particular, we focus on two-dimensional quantum dots and employ configuration-interaction techniques to directly compute the correlated many-body eigenstates of the system. We produce spatial maps of the single-particle charge and spin density and verify the annular structure of the charge density and the rotational invariance of the spin field. We further compute two-point spin correlations to determine the correlated structure of a single component of the spin vector field. In addition, we compute three-point spin-correlation functions to uncover chiral structures. We present evidence for both chiral and quasitopological spin textures within energetically degenerate subspaces in the three- and four-particle systems.

I. INTRODUCTION

The investigation of correlations among electrons confined to quantum dots (QDs) is an active area of research in condensed-matter physics due to their experimental tunability,[1,2] theoretical efficacy,[3] and application in, for example, quantum information science.[4–9] For two-dimensional QDs with circular confinement, the combination of confinement and long-range Coulomb repulsion results in charge densities peaked in annular regions about the dot center. Calculations of two-point correlation functions[10] have further revealed that these confined electrons exhibit textures akin to Wigner molecules. Numerical work has shown these behaviors to depend on the size and shape of the QD, as well as the strength of the applied magnetic field.[11]

Since the spin of confined electrons provides a viable implementation of qubits,[12,13] an understanding of the configurations and correlations formed among confined spins is crucial for the implementation of spin qubits. Furthermore, the degree of control in fabrication and manipulation of QDs makes them ideal environments for the study of fundamental behaviors of both spin and charge. In this paper, we investigate the correlations that exist between the spins of electrons trapped in circular QDs. We are specifically interested in the formation of topological spin textures that may arise due to interaction or statistical effects among the confined charges.

A significant challenge in the development of spin-based QD quantum computing is the suppression of decoherence of the spin states for time scales much longer than the time required to controllably flip a spin.[14,15] The potential to encode information using topological degrees of freedom is appealing since the enhanced stability can mitigate the burden of error correction. Various schemes which exploit a system's topological structure have been proposed.[16–19] The advantage of these is that they are *physically* fault tolerant; they are immune to local perturbations that degrade the coherent evolution of the state, a necessary ingredient in quantum computation.[20] Possible systems include two-dimensional spin models[17] (for example, atoms in an optical lattice[21]) and fractional quantum Hall systems.[18] These proposals rely on the existence of non-Abelian anyons in the excitation spectrum of the models for the information processing.

However, even in the absence of anyonic excitations, textures with topological structure are expected to be long-lived in and of themselves due to their global correlations. Since correlations decrease decoherence,[22–24] these topological structures could form an important processing element in more conventional quantum computing schemes. Even in finite-sized systems, where true topological stability likely does not occur, the relevant relaxation and decoherence times can be significantly enhanced. In Ref. 22, for example, even moderate charge correlations were sufficient to more than double the decoherence time.

Numerical work has predicted the formation of spin textures in QDs immersed in a magnetic field.[25] Experimental evidence suggests the existence of fermionic spin textures in a two-dimensional electron gas (2DEG) confined in semiconductor heterostructures,[26] vertical QDs,[27] and few-electron lateral QDs.[28,29]

A topological spin qubit would be advantageous as it could be more robust against local environmental perturbations. Nuclear magnetic resonance measurements of GaAs/AlGaAs quantum wells have shown evidence for the localization of topological skyrmion spin textures as the temperature approaches 0 K.[30,31] Recently, topological spin textures have been experimentally observed in topological insulators by means of spin-resolved angle-resolved photoemission spectroscopy.[32] The emergence of a skyrmion lattice has also been detected in the chiral magnet MnSi using neutron scattering.[33] Topological textures that are predicted to appear in QDs include vortices[34–38] and merons.[39–41] Vortices occur in the presence of a strong external magnetic field, when electron current circulates in a plane around localized regions of low electron density. Merons are topological spin textures characterized by a central "up" or "down" spin which smoothly transitions into an in-plane 2π winding along its boundary.[42] As developed in the theory, the realization of both types of quasiparticles requires the presence of an external magnetic field.

In this work, we present evidence for the existence of spin textures in circular QDs for both three-electron and four-electron systems in the absence of an external magnetic field. The electronic wave functions are calculated by configuration

interaction techniques. Two-point and three-point spin correlations are calculated in order to uncover both correlation and chirality in the spin textures which are concealed in superpositions of different configurations.

In Sec. II, we introduce our model and the foundation upon which our calculations are based. Section III describes specifically the spin correlation calculations used to examine the spin textures in the QD. We then go on to describe our results for systems of three (Sec. IV) and four (Sec. V) interacting particles. We conclude with a summary of our findings, their implications, and suggestions for further investigations in Sec. VI.

II. QUANTUM-DOT SYSTEM

Our system consists of N interacting quasiparticles of charge e, bound to a two-dimensional (2D) plane and laterally confined by a parabolic potential. The 2D Hamiltonian used to describe this "standard model" is

$$\hat{\mathcal{H}} = \sum_{i}^{N} \hat{h}_i + \frac{1}{2} \sum_{i \neq j}^{N} \frac{e^2}{\epsilon |\hat{\boldsymbol{r}}_i - \hat{\boldsymbol{r}}_j|}, \qquad (1a)$$

where ϵ is the dielectric constant of the medium and $\hat{h}$ is the single-particle Hamiltonian describing harmonic confinement,

$$\hat{h} = \frac{1}{2m^*} \left(\hat{\boldsymbol{p}} + \frac{e}{c} \widehat{\boldsymbol{A}}(\hat{\boldsymbol{r}}) \right)^2 + \frac{1}{2} m^* \omega_0^2 \hat{r}^2, \qquad (1b)$$

where m^* is the effective mass, $\hat{\boldsymbol{r}} = (\hat{x}, \hat{y})$ the position operator, and ω_0 the parabolic confinement frequency. Throughout this paper, we take the magnetic field to be zero and therefore set the vector potential $\widehat{\boldsymbol{A}}(\hat{\boldsymbol{r}}) = 0$.

Two harmonic-oscillator quantum numbers, $n, m = 0, 1, 2, \ldots$, characterize the eigenstates of the single-particle Hamiltonian[43] [Eq. (1b)]. These eigenstates are the "atomic orbitals" of the QD and are given by

$$|nm\rangle = \frac{1}{\sqrt{n! m!}} (a^\dagger)^n (b^\dagger)^m |00\rangle, \qquad (2)$$

where $a^\dagger$ and $b^\dagger$ are the usual Bose creation operators and $|00\rangle$ is the single-particle ground state. These orbitals have energy ε_{nm} given by

$$\varepsilon_{nm} = \hbar \Omega_+ \left(n + \tfrac{1}{2} \right) + \hbar \Omega_- \left(m + \tfrac{1}{2} \right), \qquad (3)$$

where $\Omega_\pm = (\sqrt{4\omega_0^2 + \omega_c^2} \pm \omega_c)/2$ and $\omega_c = e\boldsymbol{B}/(m^* c)$ is the cyclotron frequency. This energy reduces to $\hbar \omega_0 (n + m + 1)$ in the absence of a magnetic field.

The single-particle Hamiltonian, the z component of the orbital angular momentum, $\hat{L}_z$, and a component of the spin operator—which we take to be the z component $\hat{S}_z$—form a set of commuting observables which we take to classify our states: $\hat{L}_z |nms\rangle = \hbar(n - m)|nms\rangle$, $\hat{S}_z |nms\rangle = \hbar s |nms\rangle$, $\hat{h}|nms\rangle = \varepsilon_{nm}|nms\rangle$.

We are interested in spatial textures formed by the spin field, so we require the position-space representation of the orbitals.[43] These are given by[44]

$$\phi_{nm}(r,\theta) = (-1)^{n_r} \frac{1}{\sqrt{2\pi} l_0} \sqrt{\frac{n_r!}{(n_r + |m'|)!}}$$
$$\times e^{im'\theta} e^{-r^2/(4l_0^2)} \left(\frac{r}{\sqrt{2} l_0} \right)^{|m'|} L_{n_r}^{|m'|} \left(\frac{r^2}{2l_0^2} \right), \qquad (4)$$

where r and θ are the polar coordinates in two dimensions; $l_0 = \sqrt{\hbar/(2m^*\omega)}$ is the effective length with $\omega = \sqrt{4\omega_0^2 + \omega_c^2}/2$, $n' = n + m$, $m' = n - m$, $n_r = (n' - |m'|)/2$; and $L_n^{(\alpha)}(x)$ is the generalized Laguerre polynomial.[45]

The eigenstates of the interacting system are determined by exact diagonalization of Eq. (1a). This procedure begins by determining many-particle basis states (Slater determinants), eigenstates of Eq. (1b), that are composed of antisymmetrized products of the single-particle states in Eq. (2). We use 288 single-particle states and as many as 4900 many-particle basis states in the diagonalization routine. Without loss of fidelity, and for computational efficiency, the number of many-particle basis states is reduced when determining the two-point and three-point spin-correlation calculations over the range of the entire QD. Block-diagonalization is performed for a given set of parameters. These include system parameters (B, ω_0, m^*, ϵ) and the conserved quantities N, L_z, S_z, S^2. The Coulomb matrix elements are evaluated using the convenient closed-form expression derived in Ref. 46.

With the eigenstates determined, we calculate one-, two-, and three-point position-dependent spin-correlation functions over energetically degenerate manifolds. The structure of the particular operators used in these calculations is discussed in the next section.

III. PRODUCT SPIN OPERATORS

For our investigation, we require the products of up to three one-body spin operators. Here we introduce the product operators used in the calculations shown in the proceeding sections. The details associated with the derivation of each product-operator are discussed in the Appendix.

A. One-body spin operators

Except where indicated, all averages are taken over energetically degenerate manifolds. That is to say,

$$\langle A \rangle = \frac{\text{Tr}(\hat{\rho} \hat{A})}{\text{Tr}(\hat{\rho})}, \qquad (5a)$$

where the density operator $\hat{\rho}$ is defined as

$$\hat{\rho} = \sum_{i=1}^{n} |E_i\rangle \langle E_i|, \qquad (5b)$$

and where the states $|E_i\rangle$ are all the states in a given degenerate manifold of Eq. (1): $\hat{\mathcal{H}}|E_i\rangle = \text{const.}|E_i\rangle$ for all $i = 1, 2, \ldots n$.

Our analysis begins with the evaluation of both spin density and number density at position $\boldsymbol{r}$ in the QD system. We are specifically interested in isolating the spin-up and spin-down densities along the coordinate axes. Due to the conservation
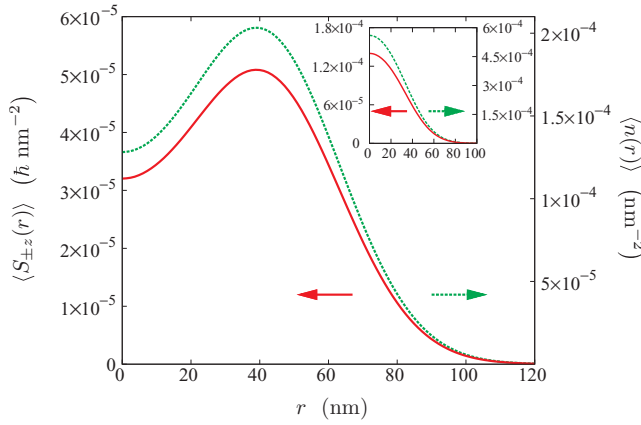
FIG. 1. (Color online) Radial dependence of the single-particle spin and number density in the three-particle ground-state manifold. (Inset) Densities in absence of Coulomb interaction. Inset axes have the same dimensions as the main plot.

of spin in the system, these one-body spin operators can only distinguish the spin-up density from the spin-down density along a single axis. We therefore define a set of spin operators $\hat{S}_{\pm z}(\boldsymbol{r})$ that separately determines the spin-up and spin-down densities along z at position $\boldsymbol{r}$. In canonical form [see Appendix Eq. (A1)], this is given by

$$\hat{S}_{sz}(\boldsymbol{r}) = \sum_{ij} U_{ijs} \hat{c}_{is}^{\dagger} \hat{c}_{js}, \qquad (6)$$

where $U_{ijs} = s\phi_i^*(\boldsymbol{r})\phi_j(\boldsymbol{r})/2$, with $s = \pm 1$ ($\hbar = 1$). Note that the composite indexes i and j each represent a set of orbital quantum numbers n and m.

The number-density and spin-density operators at position $\boldsymbol{r}$ are then given by

$$\hat{n}(\boldsymbol{r}) = \sum_{s} \hat{\psi}_s^{\dagger}(\boldsymbol{r})\hat{\psi}_s(\boldsymbol{r}) = 2(\hat{S}_{+z}(\boldsymbol{r}) + \hat{S}_{-z}(\boldsymbol{r})), \qquad (7)$$

$$\hat{S}_z(\boldsymbol{r}) = \frac{1}{2}\sum_{s} s\hat{\psi}_s^{\dagger}(\boldsymbol{r})\hat{\psi}_s(\boldsymbol{r}) = (\hat{S}_{+z}(\boldsymbol{r}) - \hat{S}_{-z}(\boldsymbol{r})), \qquad (8)$$

where $\hat{\psi}_s^{\dagger}(\boldsymbol{r})$ and $\hat{\psi}_s(\boldsymbol{r})$ are field operators that respectively create and annihilate a fermion at position $\boldsymbol{r}$, with spin s. In
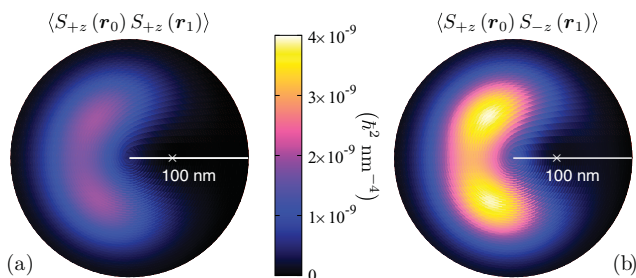

FIG. 2. (Color online) Two-point spin correlation functions for the three-particle ground-state manifold. Distributions are shown for the spin-up (a) and spin-down (b) densities at $\boldsymbol{r}_1$ given a spin-up particle at $\boldsymbol{r}_0 = (39 \text{ nm}, 0)$, denoted by a cross.
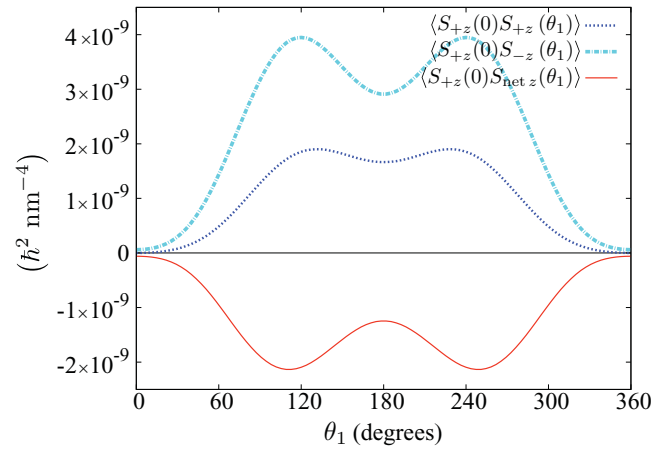

FIG. 3. (Color online) Trace along $r_{\max} = 39$ nm in the three-particle ground-state manifold, revealing the spin distribution with respect to a spin-up particle at $\boldsymbol{r}_0 = (r_{\max}, 0)$.

terms of the eigenstates $|nms\rangle$ of Eq. (1b), the field operators are given by

$$\hat{\psi}_s^{\dagger}(\boldsymbol{r}) = \sum_{nm} \phi_{nm}^*(\boldsymbol{r}) \hat{c}_{nms}^{\dagger}, \qquad (9)$$

with $\phi_{nm}(\boldsymbol{r}) = \langle \boldsymbol{r}|nm\rangle$ given in Eq. (4).

The effects of Coulomb interaction between the particles are apparent when the expectation values of the above operators are compared between the interacting and noninteracting systems.

B. Two-body spin operators

We next investigate the two-point correlations as projected onto the z axis. (Any other choice yields identical results.) Unless otherwise indicated, a spin-up (spin-down) particle
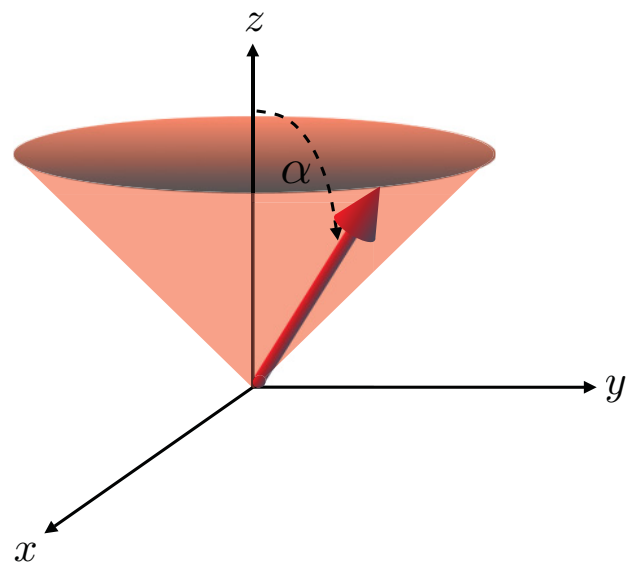

FIG. 4. (Color online) Canting angle α with respect to the axis of quantization (the z axis). The spin is not fully polarized along either the $+z$ or $-z$ axis but has components of both projections, thus smearing out along a cone of probability about the z axis.
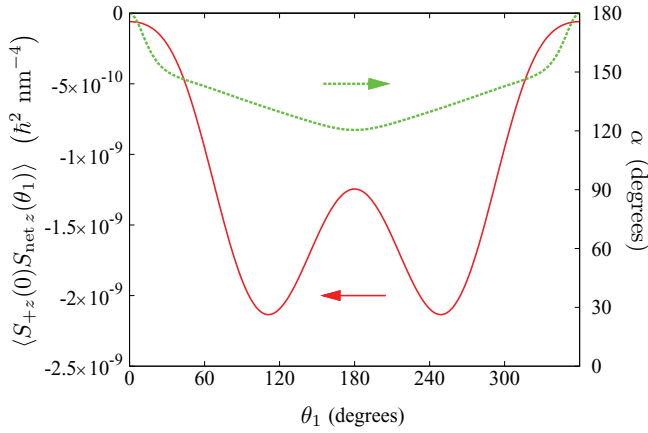
FIG. 5. (Color online) Canting angle α as a function of θ_1 along the ring of maximum single-particle density $r_{max} = 39$ nm in the three-particle ground-state manifold. The net spin density from the two-point calculation along the same ring r_{max} is shown for reference.

refers to a particle with spin polarized along the positive (negative) axis of quantization (in this work, the z axis). Specifically, we investigate $\langle S_{+z}(\boldsymbol{r}_0)S_{+z}(\boldsymbol{r}_1)\rangle$ and $\langle S_{+z}(\boldsymbol{r}_0)S_{-z}(\boldsymbol{r}_1)\rangle$. In canonical form, the operators are given by

$$\hat{S}_{+z}(\boldsymbol{r}_0)\hat{S}_{\sigma z}(\boldsymbol{r}_1) = \frac{1}{2}\sum_{ijklss'} Q_{ijkl}^{ss'\sigma}\hat{c}_{is}^{\dagger}\hat{c}_{js'}^{\dagger}\hat{c}_{ls'}\hat{c}_{ks}, \quad (10a)$$

with

$$Q_{ijkl}^{ss'\sigma} = \frac{1}{4}(\phi_i^*(\boldsymbol{r}_0)\phi_j^*(\boldsymbol{r}_1)\phi_k(\boldsymbol{r}_0)\phi_l(\boldsymbol{r}_1)\delta_{s\uparrow}\delta_{s'\sigma}$$
$$+ \phi_j^*(\boldsymbol{r}_0)\phi_i^*(\boldsymbol{r}_1)\phi_l(\boldsymbol{r}_0)\phi_k(\boldsymbol{r}_1)\delta_{s\sigma}\delta_{s'\uparrow}), \quad (10b)$$

and $\sigma = \pm 1$. As in Eq. (6), the indexes i through l in Eq. (10) are again composite indexes of pairs of orbital quantum numbers. The two-point spin correlations measure the probability of finding a particle with spin projection σz at position $\boldsymbol{r}_1$ given the existence of a particle with spin projection $+z$ at position $\boldsymbol{r}_0$.

Finally, the correlation between a spin-up particle at $\boldsymbol{r}_0$ and the *net* spin density at $\boldsymbol{r}_1$ is

$$\hat{S}_{+z}(\boldsymbol{r}_0)\hat{S}_{\mathrm{net}\,z}(\boldsymbol{r}_1) = \hat{S}_{+z}(\boldsymbol{r}_0)\hat{S}_{+z}(\boldsymbol{r}_1) - \hat{S}_{+z}(\boldsymbol{r}_0)\hat{S}_{-z}(\boldsymbol{r}_1). \quad (11)$$

These two-point spin correlations are useful for determining parallel or antiparallel spin properties such as magnetic ordering.[10] They are insufficient, however, for determining chiral textures where correlations are measured with respect to orthogonal axes. For that we turn to the three-point spin-correlation functions next.

C. Three-body spin operators

We compute three unique three-point correlations:

$$\langle S_{+x}(\boldsymbol{r}_0)S_{+y}(\boldsymbol{r}_1)S_{\mathrm{net}\,x}(\boldsymbol{r}_2)\rangle, \quad (12a)$$
$$\langle S_{+x}(\boldsymbol{r}_0)S_{+y}(\boldsymbol{r}_1)S_{\mathrm{net}\,y}(\boldsymbol{r}_2)\rangle, \quad (12b)$$

and

$$\langle S_{+x}(\boldsymbol{r}_0)S_{+y}(\boldsymbol{r}_1)S_{\mathrm{net}\,z}(\boldsymbol{r}_2)\rangle. \quad (12c)$$

These three-point spin correlations measure the probability of finding a particle with spin projected along the x, y, or z axis, respectively, given that there is a particle at position $\boldsymbol{r}_0$ that is spin-up along the x axis *and* a particle at position $\boldsymbol{r}_1$ that is spin-up along the y axis. Whereas the two-point functions can determine whether the spin projection of a second particle is parallel or antiparallel to the spin projection of the first particle, it cannot determine the orientation of the spin of the second particle in a plane other than that of the spin of the first particle. The three-point functions in Eq. (12) can indeed uncover such chiral structure. Explicitly, the three-body spin operators can be expressed as

$$\hat{S}_{+x}(\boldsymbol{r}_0)\hat{S}_{+y}(\boldsymbol{r}_1)\hat{S}_{\mathrm{net}\,x}(\boldsymbol{r}_2)$$
$$= \frac{1}{3!}\sum_{\substack{ijklmn\\s_1s_2s_3}} K_{ijklmn}^{s_1s_2s_3}\hat{c}_{is_1}^{\dagger}\hat{c}_{js_2}^{\dagger}\hat{c}_{ks_3}^{\dagger}\hat{c}_{ns_3}\hat{c}_{ms_2}\hat{c}_{ls_1}, \quad (13a)$$
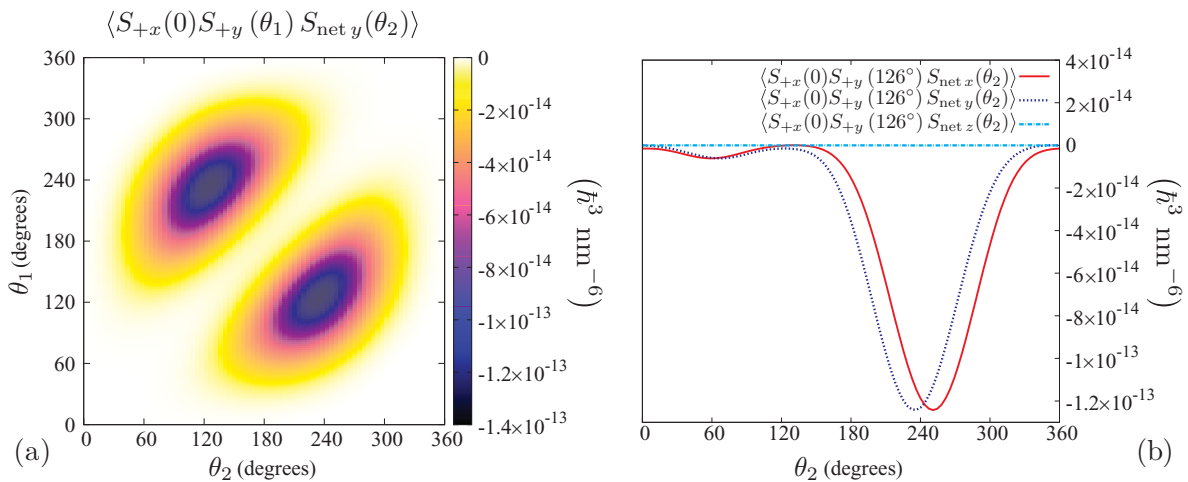

FIG. 6. (Color online) Three-point spin correlations, Eq. (12), along the ring $r_{max} = 39$ nm for the three-particle ground-state manifold. (a) The net S_y is plotted given a spin-up particle along the x-axis at $\theta_0 = 0°$ and a spin-up particle along the y axis at θ_1. (b) The three-point correlations for net spins along the x, y, and z axes for $\theta_0 = 0°$ and $\theta_1 = 126°$ on the ring r_{max}.

where

$$K_{ijklmn}^{s_1 s_2 s_3} = \frac{3}{16} \delta_{s_1 s_2} \delta_{s_2 \bar{s}_3}$$
$$\times [i s_3 \phi_i^*(\boldsymbol{r}_0) \phi_j^*(\boldsymbol{r}_1) \phi_k^*(\boldsymbol{r}_2) \phi_m(\boldsymbol{r}_0) \phi_n(\boldsymbol{r}_1) \phi_l(\boldsymbol{r}_2)$$
$$- i \phi_i^*(\boldsymbol{r}_0) \phi_k^*(\boldsymbol{r}_1) \phi_j^*(\boldsymbol{r}_2) \phi_m(\boldsymbol{r}_0) \phi_l(\boldsymbol{r}_1) \phi_n(\boldsymbol{r}_2)$$
$$- \phi_i^*(\boldsymbol{r}_0) \phi_j^*(\boldsymbol{r}_1) \phi_k^*(\boldsymbol{r}_2) \phi_n(\boldsymbol{r}_0) \phi_m(\boldsymbol{r}_1) \phi_l(\boldsymbol{r}_2)$$
$$- \phi_k^*(\boldsymbol{r}_0) \phi_i^*(\boldsymbol{r}_1) \phi_j^*(\boldsymbol{r}_2) \phi_m(\boldsymbol{r}_0) \phi_l(\boldsymbol{r}_1) \phi_n(\boldsymbol{r}_2)],$$

$$(13b)$$

and with similar expressions for the remaining two operators in Eq. (12). In Eq. (13), each of the six indexes i through n is once again a composite index over pairs of orbital quantum numbers. Furthermore, in Eq. (13b), $\bar{s}_i \equiv -s_i$, with $s_i = \pm 1$ denoting the usual spin projections.

The choice for the first two spin projections is not unique; due to the absence of a preferred spin orientation in the system, each expression is equivalent to any cyclic permutation of the spin components. We focus below on the cases where two of the three spins operators lie in the $(x\text{-}y)$ plane of the dot.

IV. THREE-PARTICLE SYSTEM

In this section, we investigate spin correlations that exist in the two lowest-lying states of a system with three charged particles. Our system is modeled with GaAs parameters ($\epsilon = 12.4$ and $m^* = 0.067 m_e$), and our confinement potential is $\omega_0 = 1.0$ meV, yielding an effective length at $B = 0$ of $l_0 = 23.8$ nm.

A. Ground-state manifold

At zero magnetic field, the ground state of the three-particle system is fourfold degenerate, with quantum numbers $L_z = \pm 1$, $S = 1/2$, and $S_z = \pm 1/2$. We compute $\langle S_{+z}(\boldsymbol{r}) \rangle$ and $\langle S_{-z}(\boldsymbol{r}) \rangle$ within this degenerate subspace [see Eq. (5)]. From these, we determine both the net density, $\langle n(\boldsymbol{r}) \rangle$ [Eq. (7)] and the net spin $\langle S_z(\boldsymbol{r}) \rangle$ [Eq. (8)]. We then go on to calculate the two-point spin functions to demonstrate correlations between parallel and antiparallel spin components, followed by the three-point functions to uncover chiral correlations.

1. Single-particle densities

To illustrate the effects of long-range Coulomb repulsions, we consider the spin density with and without interactions. In the noninteracting case, each eigenstate is a single antisymmetrized orbital configuration. For the three-particle system, there are two particles on the $|nm\rangle = |00\rangle$ orbital and one on either the $|10\rangle$ or $|01\rangle$ orbital. This yields four degenerate states with quantum numbers $(S, S_z, L_z) = (1/2, \pm 1/2, \pm 1)$. For the interacting case, these symmetries are not explicitly broken; the degeneracy and the quantum numbers remain the same, but the states themselves are now correlated, involving many other orbital configurations consistent with the symmetry.

Figure 1 shows single-particle densities for the total ground-state manifold as a function of radial distance from the center for both the interacting and noninteracting cases. There is azimuthal symmetry for these configurations due to the underlying circular symmetry of the dot itself, manifest in the Hamiltonian [Eq. (1)].
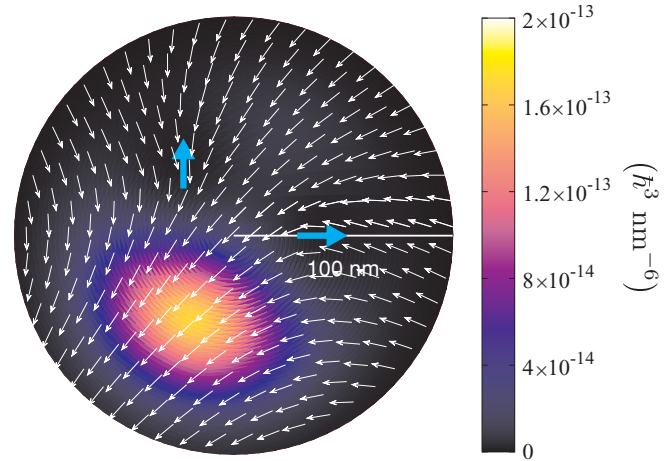

FIG. 7. (Color online) Net spin distribution in the plane of the QD for the three-particle ground-state manifold, as determined by three-point spin correlations. The magnitude is denoted by the color bar and the direction is indicated by the vector field. The z component is negligible here. The calculation is done with respect to a particle of spin-up projection on the x axis at $\boldsymbol{r}_0 = (39 \text{ nm}, 0°)$ and a particle of spin-up projection on the y axis at $\boldsymbol{r}_1 = (39 \text{ nm}, 126°)$. (These locations are denoted by the blue arrows.)

The noninteracting case is characterized as Gaussian-like with a peak at the origin. When Coulomb interactions are considered, the repulsion smears out the density over different orbital configurations.[47] The competition between repulsion and confinement results in an annular density about the origin. These interaction effects are strong; the ground-state energy of the interacting system is 10.30 meV for these experimentally-relevant system parameters—more than twice the ground-state energy of the noninteracting case (4.0 meV).

The effects of Coulomb repulsion are also reflected in the single-particle spin densities as well. Note, however, that in both cases we have $\langle S_{+z}(\boldsymbol{r}) \rangle = \langle S_{-z}(\boldsymbol{r}) \rangle$: $\langle S_{\text{net}\, z}(\boldsymbol{r}) \rangle = 0$ everywhere in the dot; therefore, the one-point calculations are insufficient for showing the Coulomb effects on spin. This is a consequence of the SU(2) symmetry present at zero magnetic field.
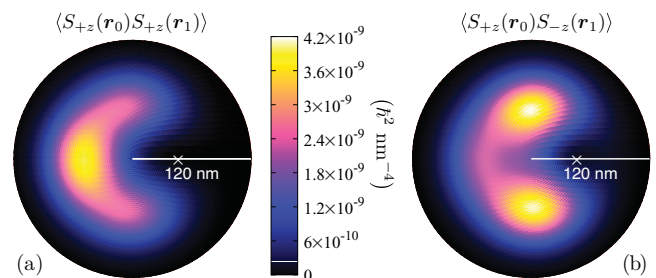

FIG. 8. (Color online) Two-point spin correlations in the four-particle ground-state manifold given a spin-up particle at $\boldsymbol{r}_0 = (48 \text{ nm}, 0)$ (white cross). The distributions are shown for the net spin-up density (a) and spin-down density (b).
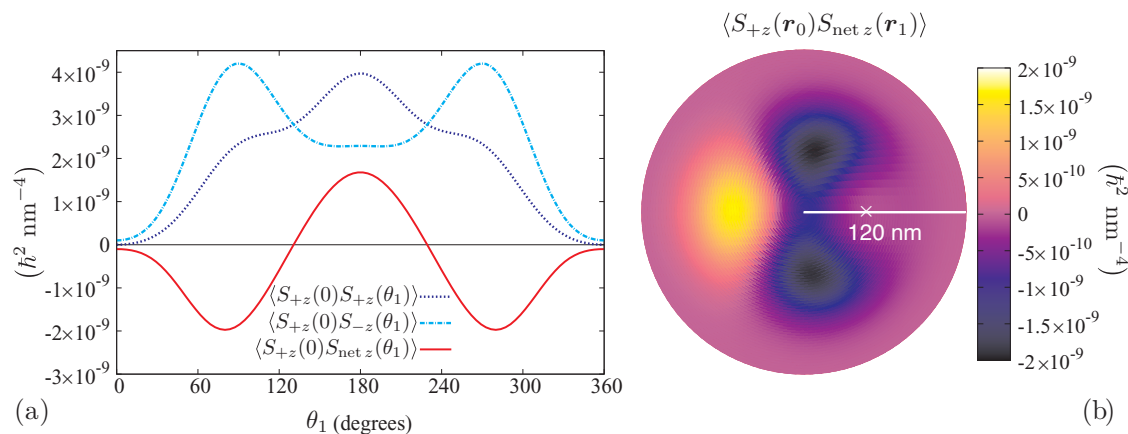
FIG. 9. (Color online) Two-point spin correlations in the four-particle ground-state manifold. (a) Trace is along the ring of maximum single-particle density $r_{max} = 48$ nm, with respect to a spin-up particle located at $\boldsymbol{r}_0 = (r_{max}, 0°)$. (b) Net spin in the QD, given a spin-up particle at $\boldsymbol{r}_0 = (r_{max}, 0°)$.

2. Two-point spin correlations

For the two-point spin correlations [Eq. (10)], we consider the case where $\boldsymbol{r}_0$ is fixed at the location of maximum single-particle density, $r_{max} \equiv 39$ nm, as obtained in the previous section. We further define the angular location of $\boldsymbol{r}_0$ to be $\theta_0 = 0$. We do not the discuss the noninteracting limit for these calculations.

The two-point correlations $\langle S_{+z}(\boldsymbol{r}_0)S_{+z}(\boldsymbol{r}_1)\rangle$ and $\langle S_{+z}(\boldsymbol{r}_0)S_{-z}(\boldsymbol{r}_1)\rangle$ for the interacting ground-state manifold are shown in Fig. 2 as a function of $\boldsymbol{r}_1$ for $\boldsymbol{r}_0 = (r_{max}, \theta_0)$. Two peaks are evident along the ring of radius r_{max}. Note that our averages [Eq. (5)] are obtained by tracing over *all* the degenerate states in the ground-state manifold. An incipient Wigner crystallization is apparent with the spins forming a classical-like lattice at the vertexes of a triangle.[10,11] This structure is not seen in the noninteracting case, implying that the Coulomb repulsion between the particles is responsible for this spin texture.

To more clearly probe the angular inhomogeneity, we plot in Fig. 3 results along the ring r_{max}. In particular, we show the
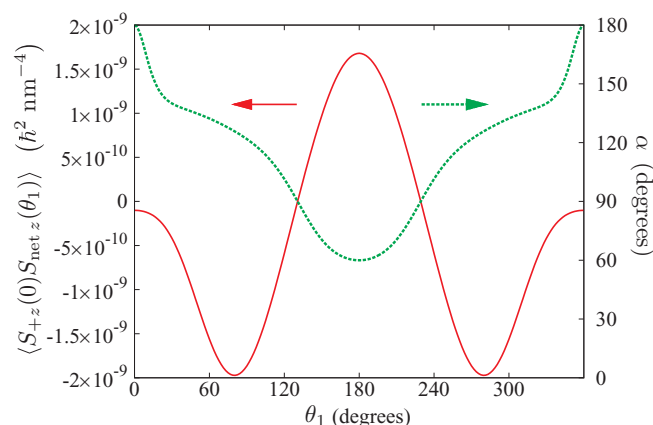

FIG. 10. (Color online) Canting angle α as a function of θ_1 along the ring of maximum single-particle density $r_{max} = 48$ nm in the four-particle ground-state manifold. The net spin density from the two-point calculation along the same ring r_{max} is shown for reference.

net spin S_z as well as the individual components $S_{\pm z}$, given a spin-up particle at $\boldsymbol{r}_0$. Note as $\boldsymbol{r}_1$ approaches $\boldsymbol{r}_0$ the remaining spin-up density goes to zero, indicative of a Pauli vortex[48] at that position. As well, the spin density at the two peaks is not fully polarized, indicating a degree of canting away from the z axis: The net spin tilts toward the x-y plane. The lack of equal magnitudes of spin-up and spin-down probabilities at every point along r_{max} in Fig. 3 indicates that the spin density never lies completely in the x-y plane. Since the spin density never crosses through the plane, it cannot have winding order. Windings are important in these spin systems as they represent clear examples of topologically stable structures.

The two-point correlations are insufficient to determine the probable orientation of the spin in the x-y plane, so the results of these calculations can be interpreted as the smearing out of the net spin across the surface of a cone centered at a local z axis at every point measured in the calculation. The opening angle of the cone is twice that of the local canting angle, the degree of tilting from the local z axis, of the spin. This cone, along with the canting angle, is illustrated in Fig. 4.

The canting angle can be determined in the following manner: If we consider the spin-density field shown in Fig. 3 as itself a spin-half field, we may generally write its local orientation as

$$|\psi(r_{max}, \theta_1)\rangle = \frac{1}{N}(c_+|+z\rangle + e^{i\beta}c_-|-z\rangle), \quad (14)$$

where $c_\pm$ are real and may be defined as

$$c_+ = \langle S_{+z}(\boldsymbol{r}_0)S_{+z}(r_{max}, \theta_1)\rangle \equiv N\cos\frac{\alpha}{2}, \quad (15a)$$

$$c_- = \langle S_{+z}(\boldsymbol{r}_0)S_{-z}(r_{max}, \theta_1)\rangle \equiv N\sin\frac{\alpha}{2}, \quad (15b)$$

and where $N = \sqrt{c_+^2 + c_-^2}$ is a local normalization. The symmetry of the two-point functions prevents discrimination of different values of the azimuthal angle β, but it *can* determine the canting angle α.

For each of the two peaks in Fig. 3, the canting angle with respect to the positive z axis is determined to be $\alpha = 131°$. That is, relative to a spin-up particle at $\boldsymbol{r}_0$, the spin-density peaks
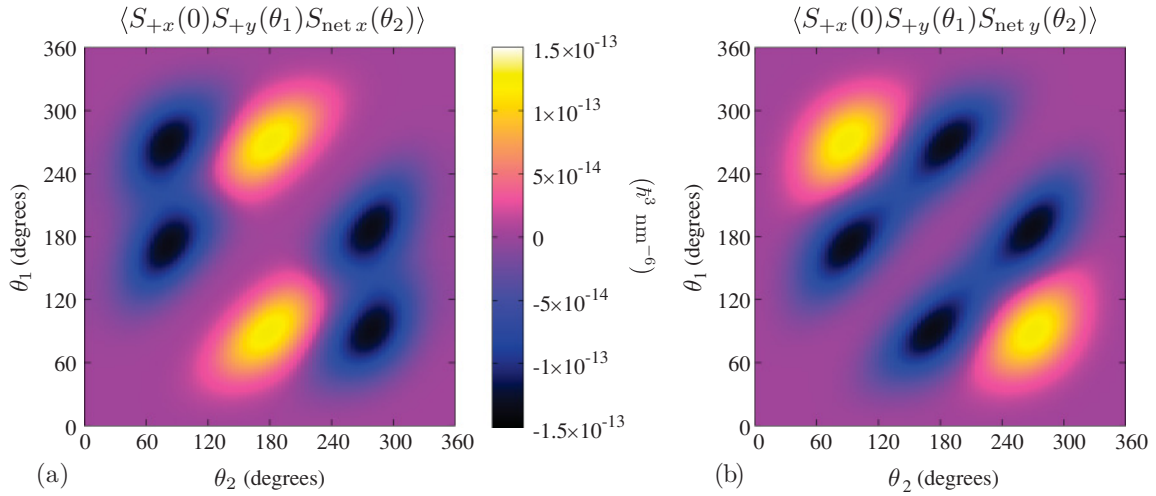
FIG. 11. (Color online) Three-point spin correlations along the ring of maximum single-particle density $r_{max} = 48$ nm for the four-particle ground state. Specifically, the net S_x (a) and net S_y (b) are determined with respect to a particle of spin-up projection along the x axis at $\boldsymbol{r}_0 = (r_{max}, 0)$ and a particle of spin-up projection along the y axis at $\boldsymbol{r}_1 = (r_{max}, \theta_1)$.

describing the other two particles both occupy the surface of a cone with canting angle $49°$ from the negative z axis. Figure 5 shows the resulting canting angle from the positive z axis of the local Bloch vector for each value of θ_1 along the ring r_{max}. The canting angle becomes greatest (α approaches $180°$) as θ_1 approaches $\theta_0 = 0$, and is a minimum at $\theta_1 = 180°$. (Pauli exclusion dictates that $\alpha \rightarrow 180°$ as $\theta_1 \rightarrow \theta_0$.)

The two-point functions in this system with SU(2) symmetry are insufficient to distinguish chiral structures. Three-point functions are necessary to resolve spin components in the plane perpendicular to the axis defined by the two-point functions. We turn to these next.

3. Three-point spin correlations

As described in Sec. III C, we compute the three distinct three-point correlation functions given in Eq. (12). Other three-point functions can be related to one of these three due to the symmetry of the underlying Hamiltonian.

In Eq. (12), we fix $\boldsymbol{r}_0$ on the ring of maximum single-particle density ($r_{max} = 39$ nm) at $\theta_0 = 0$. The correlation functions are then a function of the four variables r_1, θ_1, r_2, and θ_2. If we further choose to probe the system along the ring r_{max}, we then obtain the 2D map in the two angles θ_1 and θ_2 shown in Fig. 6(a). Explicitly, Fig. 6(a) is a plot of $\langle S_{+x}(r_{max}, 0) S_{+y}(r_{max}, \theta_1) S_{net\,y}(r_{max}, \theta_2) \rangle$ as a function of θ_1 and θ_2. As the angular location of the second spin approaches $\theta_1 = 120°$ with respect to the first spin, a peak emerges in the net spin distribution along the y axis. The maximum correlations occur at $(\theta_1, \theta_2) = (126°, 235°)$ and $(234°, 125°)$. Note the inversion symmetry about the point $(180°, 180°)$. Very similar results are seen for the net spin distribution along the x axis (not shown).

The three-point correlations for the net spin distributions along the x, y, and z axes with respect to a spin-up particle along the x axis at $\boldsymbol{r}_0 = (r_{max}, 0)$, and a spin-up particle along the y axis at $\boldsymbol{r}_1 = (r_{max}, 126°)$ are displayed in Fig. 6(b).
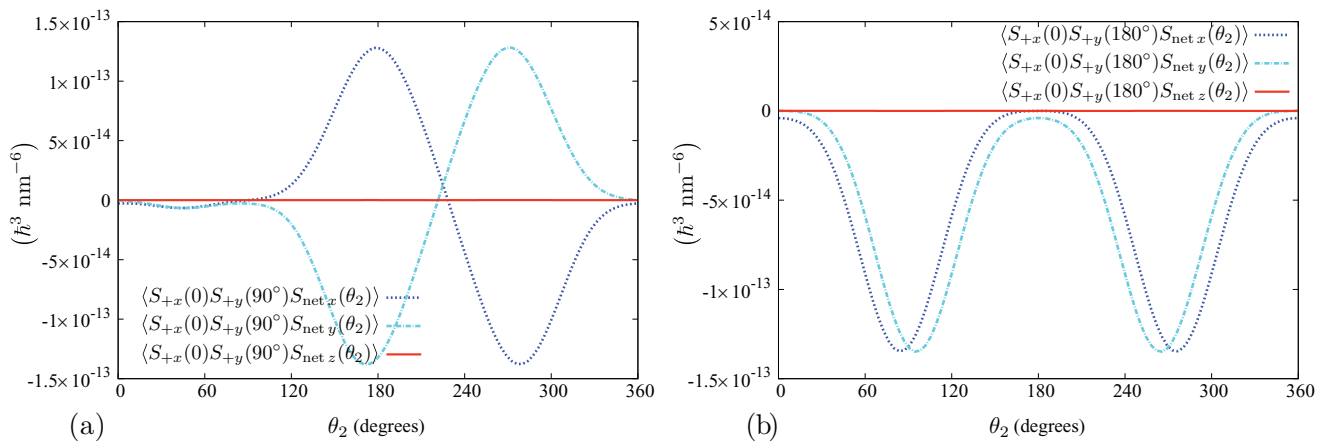

FIG. 12. (Color online) Three-point spin correlations along the ring of maximum single-particle density $r_{max} = 48$ nm in the four-particle ground-state manifold with respect to a particle that is spin-up along the x axis at $\boldsymbol{r}_0 = (r_{max}, 0)$ and a particle that is spin-up along the y axis at $\boldsymbol{r}_1 = (r_{max}, 90°)$ (a) and $\boldsymbol{r}_1 = (r_{max}, 180°)$ (b).
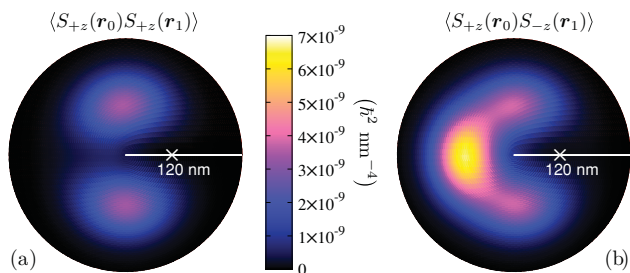
FIG. 13. (Color online) Two-point spin correlations in the first excited state of the four-particle system with respect to a spin-up particle at $r_0 = (48\text{ nm}, 0)$ (white cross). Shown are the spin-up (a) and spin-down (b) distributions.

Note the net spin distribution along the z axis is negligible in comparison to the distributions along the x and y axes: Any spin density that remains in the system lies only in the plane of the two spins at r_0 and r_1, respectively.

Figure 7 is a map of the net spin distribution in the three-particle ground-state manifold, given a spin-up particle along x at $r_0 = (r_{max}, 0)$ and a spin-up particle along y at $r_1 = (r_{max}, 126°)$. The peak along the ring r_{max} occurs at $\theta_3 = 243°$, and the net spin at this peak has an equal spin-down projection along both the x and the y axes. Note in this distribution the peak of the net spin density and the two locations r_0 and r_1 are each equidistant from each other.

The three-point correlations suggest that the most probable spin configuration in this three-particle state has a planar, splayed order, as seen in Fig. 7. Recall, however, that the results from the two-point correlations imply that the state does not have a clear winding order.

B. First excited state

Like the three-particle ground state, the first excited state is also fourfold degenerate. However, in contrast to the ground-state manifold, $L_z = 0$ for all four degenerate states in the first excited state. Degeneracy occurs through the spin quantum numbers $S = 3/2$ and $S_z = \pm 3/2, \pm 1/2$.
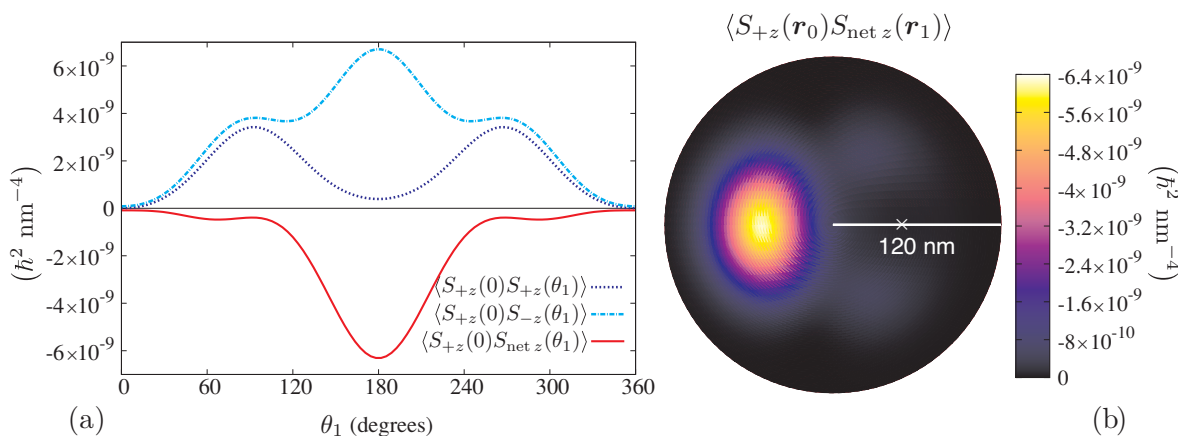
As in the ground state, the single-particle-density and the spin-density distributions are rotationally symmetric. When interactions are considered, the annular distributions peak at $r_{max} \equiv 41$ nm. These distributions are similar to those seen in Fig. 1 for the ground state and are not shown. As seen in the ground-state manifold, the net S_z is once again zero everywhere in the QD for both the interacting and the noninteracting cases. The noninteracting limit is not investigated further.

The two-point spin correlations in the interacting first excited state are similar to those seen for the interacting ground state (see Fig. 2); namely, there are two peaks along the ring r_{max}. The two-point distribution also shows canting toward the x-y plane with respect to a spin-up particle at $r_0 \equiv (r_{max}, 0)$. Unlike the ground state, this canting is constant for all θ along the ring r_{max} except at a very small region about $\theta = 0$ in accordance with Pauli exclusion and has a value of $\alpha = 53°$. Once again a Pauli vortex is present at r_0.

We turn now briefly to the three-point spin correlations in the first excited state along the ring r_{max}. We fix one spin-up particle along the x axis at $\theta_0 = 0°$, and the other spin-up particle along the y axis at $\theta_1 = 120°$, the location of one of the two peaks determined by the two-point correlation calculation. Due to the spin-polarized states, minor differences exist between this manifold and the ground-state manifold, but otherwise these results are very similar and so results for the excited-state manifold are not shown.

V. FOUR-PARTICLE SYSTEM

We examine the lowest two energy eigenstates in a system of four charged particles for the same system parameters used above. We begin the investigation of the four-particle system by first determining the radial location of maximum single-particle density in each state. With this established, we calculate higher-order spin correlations in this region.

A. Ground state

The ground state of the four-particle system is threefold degenerate with quantum numbers $L_z = 0$, $S = 1$, and

FIG. 14. (Color online) (a) Trace of the two-point spin distribution along the ring $r_{max} = 48$ nm with respect to a spin-up particle at $r_0 = (48\text{ nm}, 0)$ in the four-particle first excited state. (b) Net two-point distribution of S_z throughout the QD for the same state.
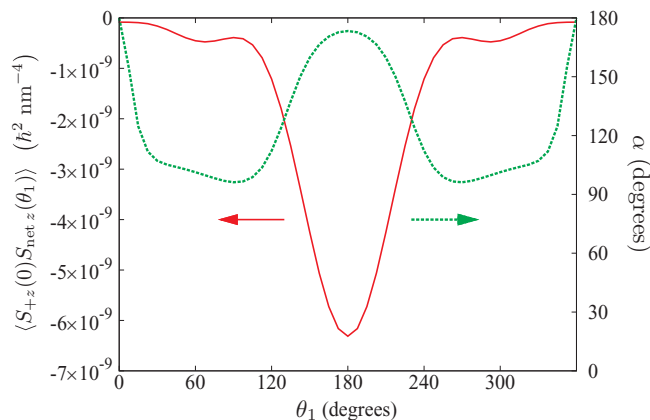
FIG. 15. (Color online) Canting angle α as a function of θ_1 along the ring $r_{max} = 48$ nm in the four-particle first excited state. The net spin density from the two-point calculation along the same ring r_{max} is shown for reference.

$S_z = \pm 1, 0$. The single-particle density distribution in the ground-state manifold (not shown) is annular in shape with a peak at $r_{max} \equiv 48$ nm from the center of the dot. This distance is greater than in the three-particle states primarily due to the additional Coulomb repulsion present in the system.

The two-point spin correlations in the four-particle ground state are calculated with respect to a spin-up particle at $r_0 \equiv (r_{max}, 0)$. The calculations are similar to those for the three-particle system. Figure 8 shows the distribution of the remaining spin-up density and spin-down density in the ground-state manifold with respect to the spin-up particle at r_0. As seen in the three-particle ground state, there is a Pauli vortex at r_0. Figure 8(a) shows that the probability of finding another spin-up particle is strongest at $\theta_1 = 180°$. Conversely, the spin-down distribution in Fig. 8(b) shows two peaks, one at $\theta_1 = 90°$ and the other at $\theta_1 = 270°$. The saddle point at $\theta_1 = 180°$ is more than half of the magnitude of the peaks. Taken together, the two plots in Fig. 8 indicate

an antiferromagnetic alignment of the spins, with each spin equidistant from each other, distributed along the ring of maximum single-particle density. This is further revealed in the net spin distribution, shown in Fig. 9. Figure 9(b) shows the evident antiferromagnetic tendency in the four-particle ground-state manifold. However, as shown in Fig. 9(a), in this small system, the spins are neither fully localized nor fully polarized in the QD.

In the four-particle ground-state manifold, the net spin density from the two-point calculation shows canting along the ring r_{max} as a function of θ_1 similar to that in the three-particle ground-state manifold. The canting angle becomes antiparallel ($\alpha = 180°$) relative to the spin-up particle at $r_0 = (r_{max}, 0)$ as θ_1 approaches zero, passing through the x-y plane when the net spin density from the two-point function is zero along the ring r_{max} (near $\theta_1 = 130°$ and $\theta_1 = 230°$), and has a positive projection on the z axis at $\theta_1 = 180°$, where the two-point function shows the net spin density to be predominantly spin-up. The canting angle along r_{max} is consistent with the antiferromagnetic ordering suggested by the two-point correlation calculations. The result is shown in Fig. 10.

To investigate possible chiral textures, we examine three-point spin correlations in the four-particle ground-state manifold with respect to one-particle spin-up along the x axis at r_0 and a second-particle spin-up along the y axis at $r_1 \equiv (r_{max}, \theta_1)$. Figure 11(a) shows the net x spin distribution and Fig. 11(b) shows the net y spin distribution in the system at every angular position θ_2 as a function of θ_1. (The net z correlations are negligible and are not shown.)

As θ_1 approaches $90°$, two peaks (the two remaining particles) emerge in the net x and y spin distributions at $\theta_2 = 180°$ and $\theta_2 = 270°$. As θ_1 approaches $180°$, two different peaks arise at $\theta_2 = 90°$ and $\theta_2 = 270°$. There is a third region, at $\theta_1 = 270°$ of large correlation that mirrors that at $\theta_1 = 90°$. Note the inversion symmetry through the point $(\theta_1, \theta_2) = (180°, 180°)$. Figure 12 focuses on the two regions of large correlation, when $\theta_1 = 90°$ and $180°$, showing the net x, y, and z spin distributions as a function of θ_2.

$$\langle S_{+x}(0)S_{+y}(\theta_1)S_{net\,x}(\theta_2)\rangle$$

(a)

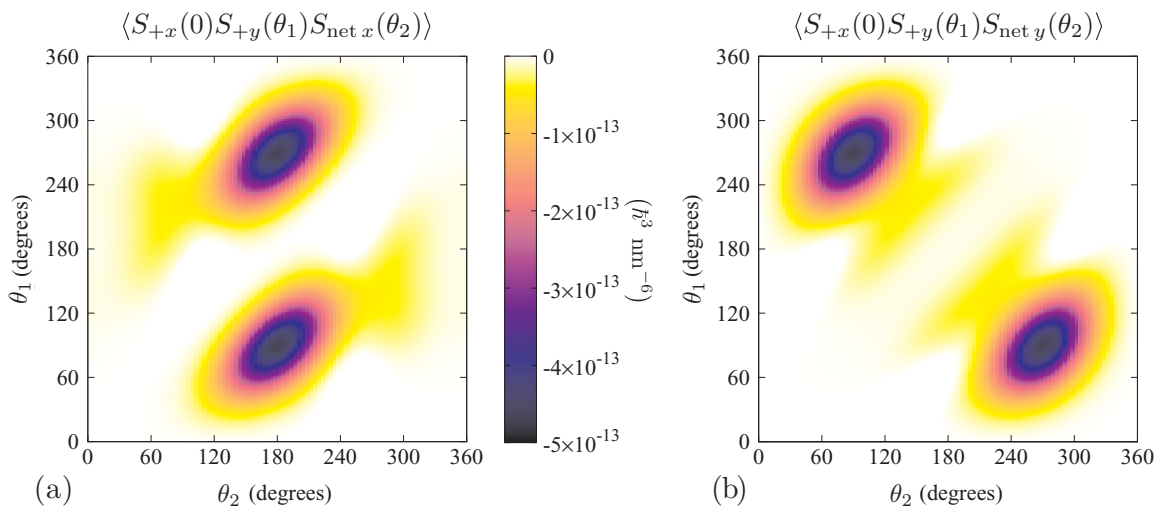$$\langle S_{+x}(0)S_{+y}(\theta_1)S_{net\,y}(\theta_2)\rangle$$

(b)

FIG. 16. (Color online) Three-point correlations along the ring $r_{max} = 48$ nm in the four-particle first excited state with respect to a spin-up particle along the x axis at $r_0 = (r_{max}, 0)$ and a spin-up particle along the y axis at $r_1 = (r_{max}, \theta_1)$. Shown are the spin distributions along $r_2 = (r_{max}, \theta_2)$ for the net spin along the x axis (a) and along the y axis (b).
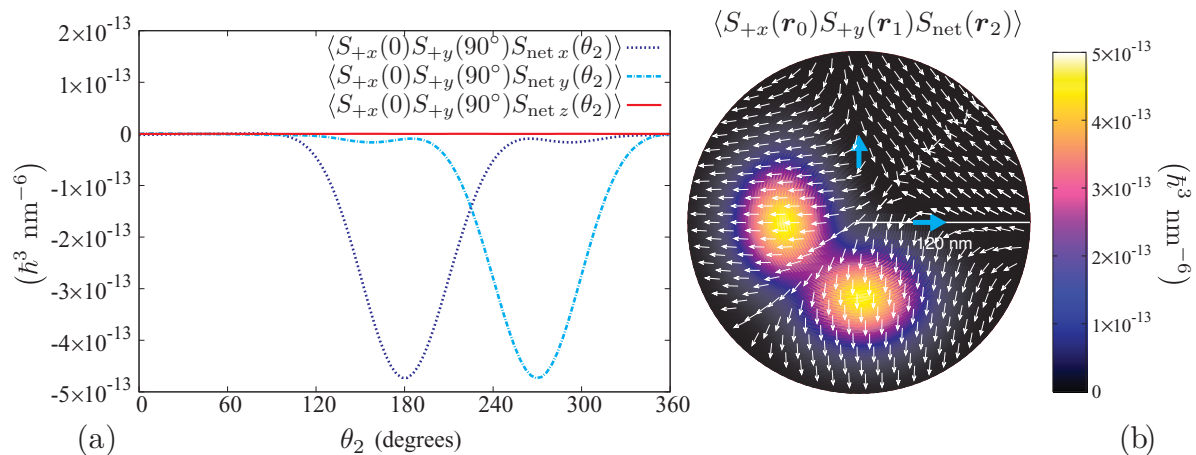
FIG. 17. (Color online) (a) Trace along the ring r_{max}, revealing the net spin distributions in the four-particle first excited state given a spin-up particle along x at $\boldsymbol{r}_0 = (r_{max}, 0)$ and a spin-up particle along y at $\boldsymbol{r}_1 = (r_{max}, 90°)$. (b) The corresponding net spin distribution in the plane of the QD. The vector field depicts the orientation and the color depicts the magnitude. The locations $\boldsymbol{r}_0$ and $\boldsymbol{r}_1$ are indicated by the blue arrows.

From these plots we conclude that chiral spin structures exist in the ground-state manifold of the interacting four-particle system, but the structures cannot be readily characterized by a definite winding about any axis.

We now go on to consider the lowest-energy excitation above this ground-state manifold, where we *do* uncover winding textures.

B. First excited state

The first excited state in the four-particle system is nondegenerate with quantum numbers $L_z = 0$, $S = 0$. It too has a circularly symmetric single-particle density distribution about the origin, with a peak at $r_{max} \equiv 48$ nm.

Figure 13 shows the two-point spin correlations throughout the plane of the dot with respect to a spin-up particle at $\boldsymbol{r}_0 \equiv (r_{max}, 0)$. The distribution of the spin-up and spin-down densities are shown. The spin-up density shown in Fig. 13(a) contains two peaks at $\theta_1 = 90°$ and $\theta_1 = 270°$, both along the ring r_{max}. The probability drops to approximately one-tenth of its magnitude between the peaks, at $\theta_1 = 180°$. The spin density goes to zero as $\boldsymbol{r}_1$ approaches $\boldsymbol{r}_0$, giving evidence for a Pauli vortex at $\boldsymbol{r}_0$. The spin-down density shown in Fig. 13(b) has three peaks, the largest at $\theta_1 = 180°$, and two smaller ones of equal magnitude at $\theta_1 = 90°$ and $\theta_1 = 270°$. In contrast to the ground state (see Fig. 8), this manifold does not exhibit antiferromagnetic order.

The two smaller peaks in the spin-down distribution are approximately half the magnitude of the large peak and

approximately equal to the magnitude of the two peaks in the spin-up distribution. The net S_z distribution at $\theta_1 = 90°$ and $\theta_1 = 270°$ is therefore approximately zero, indicating an in-plane orientation. This is further evident in the trace along the ring r_{max} shown in Fig. 14(a) and the net spin distribution shown in Fig. 14(b).

The single peak at $\theta_1 = 180°$ is composed primarily of a single spin species. These results are consistent with two-point spin correlations in Ref. 10. Of note here is that, in the transition from spin-up at $\theta_1 = 0°$ to spin-down at $\theta_1 = 180°$, the spin lies almost completely in the plane of the QD. Calculation of the canting angle along the ring r_{max} as a function of θ_1 is plotted in Fig. 15. In this case there are two locations where the net spin has the greatest canting. Relative to the spin-up particle at $\boldsymbol{r}_0 = (r_{max}, 0)$, as θ_1 approaches $\theta_0 = 0$ and also as θ_1 approaches $180°$, the canting angle approaches $180°$. In the regions along r_{max} where the net spin distribution is almost zero, the canting angle approaches $90°$, showing that the net spin exists in the x-y plane. However, the two-point correlation function is incapable of determining the orientation of the spin within the plane. We therefore turn to the three-point correlation function in order to determine the orientation of the in-plane spin component as it transitions between spin-up and spin-down.

We calculate three-point spin correlations along the ring r_{max} with respect to a spin-up particle along the x axis at $\boldsymbol{r}_0 = (r_{max}, 0)$ and a spin-up particle along the y axis at $\boldsymbol{r}_1 = (r_{max}, \theta_1)$. The net x and net y spin distributions are shown in Fig. 16 as a function of θ_1 and θ_2.

TABLE I. Summary of textures uncovered in the respective degenerate manifolds.

Manifold	Single-particle densities	Two-point	Three-point	Canting
Three-particle ground state	$r_{max} = 39$ nm	Triangular lattice	Splayed	131°[a]
Three-particle first excited state	$r_{max} = 41$ nm	Triangular lattice	Splayed	53°
Four-particle ground state	$r_{max} = 48$ nm	Antiferromagnetic order	No winding	Varies
Four-particle excited state	$r_{max} = 48$ nm	In-plane configuration	In-plane winding	Varies

[a]At peaks.

These distributions reveal strong correlations at $\theta_1 = 90°$ and $\theta_1 = 270°$, consistent with the previous two-point correlation. Note the inversion symmetry about the point $(\theta_1, \theta_2) = (180°, 180°)$. The plots further show that for $\theta_1 = 90°$ (270°), the net spin is predominantly spin-down along x at $\theta_2 = 180°$ and predominantly spin-down along y at $\theta_2 = 270°$ (90°). Focusing attention to the case of $\theta_1 = 90°$, we plot in Fig. 17(a) the spin distribution along the ring r_{max} given a spin-up particle along x at $\theta_0 = 0°$ and a spin-up particle along y at $\theta_1 = 90°$. Figure 17(b) shows the effect of this correlation on the net spin distribution throughout the plane of the QD.

These results for the net x and y spin distributions are consistent with the z distributions calculated by the two-point correlations (see Fig. 14). Those two-point correlations revealed a single peak at 180° indicating a spin antialigned to the one at $\theta_0 = 0$ along the ring r_{max}. The three-point function with respect to a spin-up particle along x at $\boldsymbol{r}_0 = (r_{max}, 0)$ and a spin-up particle along y at $\boldsymbol{r}_1 = (r_{max}, 90°)$ yields a net spin polarized along the negative x axis at $\theta = 180°$ and a net spin polarized along the negative y axis at $\theta = 270°$, on the ring r_{max}. This is evidence of a winding along the ring r_{max}. From the symmetry of our correlation operators [Eq. (13a)], we can deduce that there are, in fact, four orthogonal windings that wind about the origin in this manner: two which begin with a particle spin-up along the x axis at $\boldsymbol{r}_0 = (r_{max}, 0)$ and then differ in the direction of their spin polarization along the y axis at $\boldsymbol{r}_1 = (r_{max}, 90°)$ (i.e., in the chirality of the rotation) and two which begin with a particle spin-down along the x axis at $\boldsymbol{r}_0 = (r_{max}, 0)$, and again differ in their chirality along the ring r_{max}. Thus, we can characterize the first excited state of the four-particle droplet as a superposition of four different windings, differing by their chirality (clockwise and counterclockwise) and by a topological charge (± 1). (See Ref. 49 for a thorough semiclassical description).

VI. SUMMARY

We have computed spin correlations in the two lowest-lying states of three-particle and four-particle circular 2D QDs to resolve spin textures that exist in the system in the presence of strong, long-range Coulomb repulsion at zero magnetic field. Our findings are summarized in Table I.

From the one-point correlation, we determine the annular regions of maximum spin density in the QD. As expected, the radial distance of this region from the origin depends on the number of confined particles and on the strength of the Coulomb repulsion.

We further compute two-point spin-correlation functions to determine the correlations in the spin field along a given direction. Each resulting spin distribution is symmetric through the diameter of the QD on which one particle is located. The details of the spin configurations are dependent on the unique quantum characteristics of the state, particularly the spin and orbital angular momentum quantum numbers. The two-point correlation calculations for each state suggest the presence of a Pauli vortex at the position of the fixed particle. In addition, these results reveal an incipient Wigner phase in the states examined above.

To uncover chiral textures, the three-point spin correlations are calculated. We plot the spin density with respect to two

particles with mutually perpendicular spins. The three-particle states we have investigated exhibit splayed textures. The four-particle ground state exhibits an antiferromagnetic texture, and the first excited state exhibits winding textures. Here the results indicate that, given a particle with spin at a point in the dot, the spin field rotates through a plane perpendicular to the original spin orientation with a full 2π winding as one moves along a closed trajectory about the origin. Importantly, given the finite size of the system and the full O(3) spin symmetry present, these winding textures are only quasitopological in character. The rotational spin symmetry, in particular, allows the spins to continually deform into the trivial texture (or, rather, to the ground-state texture). In a larger, semiclassical system with at least uniaxial anisotropy, the analogous textures *will* have topological character. In fact, in 2DEGs and bulk systems, skyrmions, and other spin textures have been shown to exist.[26,30–33]

In the present small but fully quantum system, incipient topological structures may manifest themselves if a coupling were introduced between the spin field and the spatial orientation of the QD itself, analogous to the anisotropies typically found in much larger magnetic systems. This could come about through spin-orbit coupling. There is evidence that such a coupling may break the degeneracy between the spin-winding states.[50] Together with the strong Coulomb repulsion present in these small quantum systems, the chiral structures that emerge should exhibit longer lifetimes and lower decoherence rates than their more conventional counterparts.

Improvements in the lifetime of these states could be determined, for example, by comparing the relaxation rates of the states at and away from their degeneracy point by use of single-shot measurements.[51,52] Experimental methods exist for differentiating between fully polarized spin states and correlated spin texture states in the ground state of a QD by measuring the excitation spectra of the QD as a function of magnetic field.[27–29] These methods can be used to determine when a spin texture state is present in the system. The issues of spin-orbit coupling and state lifetimes will be investigated in future work.

APPENDIX: DERIVATION OF PRODUCT SPIN OPERATORS

In this Appendix we discuss the general properties of the product-operators used in our above analysis, as well as the details associated with the derivation of each product operator.

1. One-body spin operators

A general one-body operator is expressed in canonical second-quantized form as

$$\hat{U} = \sum_{\alpha \beta} U_{\alpha\beta} \, \hat{c}_\alpha^\dagger \, \hat{c}_\beta, \qquad (A1)$$

where $U_{\alpha\beta} = (\alpha|\hat{U}|\beta)$ is a matrix element of the operator[53] and $\hat{c}_\alpha^\dagger$ and $\hat{c}_\alpha$ are second-quantized Fermi operators, respectively creating and destroying a particle in state $|\alpha\rangle$.

For a system of spin-1/2 fermions, the operator for the spin density at position $\boldsymbol{r}$ is given by ($\hbar = 1$)

$$\widehat{\boldsymbol{S}}(\boldsymbol{r}) = \frac{1}{2}\sum_{ss'}\hat{\psi}_s^\dagger(\boldsymbol{r})\widehat{\boldsymbol{\sigma}}^{ss'}\hat{\psi}_{s'}(\boldsymbol{r}), \tag{A2}$$

where $\widehat{\boldsymbol{\sigma}} = (\hat{\sigma}_x, \hat{\sigma}_y, \hat{\sigma}_z)$ are the Pauli spin matrices and $\hat{\psi}_s^\dagger(\boldsymbol{r})$ and $\hat{\psi}_s(\boldsymbol{r})$ are the field operators.

Equation (A2) yields the net spin density at point $\boldsymbol{r}$. We are additionally interested in distinguishing the spin-up and spin-down densities along each coordinate axis. We define a general set of spin operators $\hat{S}_{\pm\alpha}(\boldsymbol{r})$ that separately determines the spin-up and spin-down densities along $\alpha = x, y, z$ at position $\boldsymbol{r}$. In the S_z basis, the operator for the $\pm x$ spin density, for example, is given by

$$\hat{S}_{\pm x}(\boldsymbol{r}) = \tfrac{1}{4}[(\hat{\psi}_\uparrow^\dagger(\boldsymbol{r})\hat{\psi}_\uparrow(\boldsymbol{r}) + \hat{\psi}_\downarrow^\dagger(\boldsymbol{r})\hat{\psi}_\downarrow(\boldsymbol{r}))$$
$$\pm(\hat{\psi}_\uparrow^\dagger(\boldsymbol{r})\hat{\psi}_\downarrow(\boldsymbol{r}) + \hat{\psi}_\downarrow^\dagger(\boldsymbol{r})\hat{\psi}_\uparrow(\boldsymbol{r}))]. \tag{A3}$$

This operator can be derived from the field operators, $\hat{\psi}_{\pm x}^\dagger(\boldsymbol{r}) = [\hat{\psi}_\uparrow^\dagger(\boldsymbol{r}) \pm \hat{\psi}_\downarrow^\dagger(\boldsymbol{r})]/\sqrt{2}$, and $\hat{S}_{\pm x}(\boldsymbol{r}) = \hat{\psi}_{\pm x}^\dagger(\boldsymbol{r})\hat{\psi}_{\pm x}(\boldsymbol{r})/2$. Similarly, the operators along the other two orthogonal directions are

$$\hat{S}_{\pm y}(\boldsymbol{r}) = \tfrac{1}{4}[(\hat{\psi}_\uparrow^\dagger(\boldsymbol{r})\hat{\psi}_\uparrow(\boldsymbol{r}) + \hat{\psi}_\downarrow^\dagger(\boldsymbol{r})\hat{\psi}_\downarrow(\boldsymbol{r}))$$
$$\pm i(\hat{\psi}_\downarrow^\dagger(\boldsymbol{r})\hat{\psi}_\uparrow(\boldsymbol{r}) - \hat{\psi}_\uparrow^\dagger(\boldsymbol{r})\hat{\psi}_\downarrow(\boldsymbol{r}))] \tag{A4}$$

and

$$\hat{S}_{+z}(\boldsymbol{r}) = \tfrac{1}{2}\hat{\psi}_\uparrow^\dagger(\boldsymbol{r})\hat{\psi}_\uparrow(\boldsymbol{r}), \quad \hat{S}_{-z}(\boldsymbol{r}) = \tfrac{1}{2}\hat{\psi}_\downarrow^\dagger(\boldsymbol{r})\hat{\psi}_\downarrow(\boldsymbol{r}). \tag{A5}$$

By defining the net spin along an axis to be the difference between the spin-up and the spin-down density along that same axis [$\hat{S}_x(\boldsymbol{r}) = \hat{S}_{+x}(\boldsymbol{r}) - \hat{S}_{-x}(\boldsymbol{r})$, etc.], we obtain the components of Eq. (A2). Upon integrating these net spin components over all space, we recover the usual expressions $\hat{S}_x = (\hat{S}_+ + \hat{S}_-)/2$, $\hat{S}_y = (\hat{S}_+ - \hat{S}_-)/(2i)$, and $\hat{S}_z = (\hat{S}_\uparrow - \hat{S}_\downarrow)/2$, where $\hat{S}_+$ and $\hat{S}_-$ are S_z raising and lowering operators, respectively.

The operators in Eqs. (A3) and (A4) each contain terms which flip spins. However, since the Hamiltonian [Eq. (1)] conserves spin, and since we include spin quantum numbers to classify our states, these terms give zero contribution to Eq. (5a) for one-body spin operators. As a consequence of spin conservation we have for any degenerate manifold at zero magnetic field $\langle S_x(\boldsymbol{r})\rangle = \langle S_y(\boldsymbol{r})\rangle = \langle S_z(\boldsymbol{r})\rangle = 0$. Along the quantization (z) axis, we can distinguish between the spin-up and the spin-down density at position $\boldsymbol{r}$, but we cannot distinguish between the spin-up and spin-down density along

the two orthogonal directions: Formally, $\langle S_{+x}(\boldsymbol{r})\rangle = \langle S_{-x}(\boldsymbol{r})\rangle$, and similarly for the y direction. Consequently, it suffices to calculate only the one-point correlations of $\hat{S}_{\pm z}(\boldsymbol{r})$, as in Eq. (6).

2. Two-body spin operators

To investigate correlations along a particular axis, the two-point correlations functions are required. On physical grounds, we require that operators be symmetric in their indexes.[53] For one-body operators, we require that $U_{\alpha\beta} = U_{\beta\alpha}$. For a two-body operator, we similarly require that $V_{\alpha\beta\gamma\delta} = V_{\beta\alpha\delta\gamma}$. In general, a product of N one-body operators is not an N-body operator. Let $\hat{U}$ and $\hat{V}$ each be a one-body operator. Their product can be written as

$$\hat{U}\hat{V} = \sum_{ij}(UV)_{ij}\,\hat{c}_i^\dagger\hat{c}_j + \frac{1}{2}\sum_{ijkl}(U_{ik}V_{jl} + U_{jl}V_{ik})\hat{c}_i^\dagger\hat{c}_j^\dagger\hat{c}_l\hat{c}_k, \tag{A6}$$

where $(UV)_{ij} \equiv (i|\hat{U}\hat{V}|j)$ and $U_{ik}V_{jl} \equiv (i|\hat{U}|k)(j|\hat{V}|l)$. The product of two one-body operators is, in fact, a sum of canonical one-body and two-body operators.

There is no preferred axis along which to calculate our two-point correlations because the net spin in each degenerate manifold is zero, but one may exploit the symmetry; for example, the correlation between a spin-up particle and the remaining spin-up distribution is identical to the correlation between a spin-down particle and the remaining spin-down distribution. In general, the correlations between a particle with spin and the remaining particles of parallel spin will be the same for any orientation, as will the correlations between a particle with spin and the remaining particles of antiparallel spin. Due to spin conservation, two-point correlations between particles with perpendicular spin do not provide additional correlation information and are therefore not considered.

The two-point correlations investigated above are $\langle S_{+z}(\boldsymbol{r}_0)S_{+z}(\boldsymbol{r}_1)\rangle$ and $\langle S_{+z}(\boldsymbol{r}_0)S_{-z}(\boldsymbol{r}_1)\rangle$ in Eq. (10). With the condition $\boldsymbol{r}_0 \neq \boldsymbol{r}_1$ (while still allowing $\boldsymbol{r}_0 \to \boldsymbol{r}_1$), the one-body term vanishes. As described in Sec. A1, spin symmetry implies that all four of $\langle S_{+z}(\boldsymbol{r}_0)S_{\pm x}(\boldsymbol{r}_1)\rangle$ and $\langle S_{+z}(\boldsymbol{r}_0)S_{\pm y}(\boldsymbol{r}_1)\rangle$ are identical and equal to $\langle(S_{+z}(\boldsymbol{r}_0)S_{+z}(\boldsymbol{r}_1) + S_{+z}(\boldsymbol{r}_0)S_{-z}(\boldsymbol{r}_1))\rangle/2$.

3. Three-body spin operators

To probe for chiral textures, we compute the three-point correlation functions. These are a product of three one-body operators. In canonical form, the product of three one-body operators is the sum of a canonical one-body, two-body, and three-body operator,

$$\hat{U}\hat{V}\hat{W} = \sum_{ij}(UVW)_{ij}\hat{c}_i^\dagger\hat{c}_j + \frac{1}{2}\sum_{ijkl}((UV)_{ik}W_{jl} + U_{ik}(VW)_{kl} + (UW)_{ik}V_{kl} + (UV)_{jl}W_{ik} + U_{jl}(VW)_{ik} + (UW)_{jl}V_{ik})\hat{c}_i^\dagger\hat{c}_j^\dagger\hat{c}_l\hat{c}_k$$
$$+ \frac{1}{3!}\sum_{\substack{ijk\\lmn}}(U_{il}V_{jm}W_{kn} + U_{il}V_{kn}W_{jm} + U_{jm}V_{il}W_{kn} + U_{jm}V_{kn}W_{il} + U_{kn}V_{il}W_{jm} + U_{kn}V_{jm}W_{il})\hat{c}_i^\dagger\hat{c}_j^\dagger\hat{c}_k^\dagger\hat{c}_n\hat{c}_m\hat{c}_l, \tag{A7}$$

where $(UVW)_{ij} = (i|\hat{U}\hat{V}\hat{W}|j)$. Each of the matrix elements in Eq. (A7) is symmetric under appropriate interchange of indexes; for a three-body matrix element V_{ijklmn}, for example, we require $V_{ijklmn} = V_{ikjlnm}$, and so on.

We express our three-point correlation operators in the symmetric form shown in Eq. (A7). As in Sec. A2, spin symmetry implies that the one-body and two-body pieces of Eq. (A7) vanish when r_0, r_1, and r_2 are all different. Because our averages are taken with respect to spin-conserving states, we need only consider terms in the correlation function which themselves conserve spin. We can thus write the product operators as they are given in Eq. (13).

*http://quantum.phys.dal.ca

[1] L. P. Kouwenhoven, D. G. Austing, and S. Tarucha, Rep. Prog. Phys. **64**, 701 (2001).

[2] T. J. Bukowski and J. H. Simmons, Crit. Rev. Solid State **27**, 119 (2002).

[3] S. M. Reimann and M. Manninen, Rev. Mod. Phys. **74**, 1283 (2002).

[4] G. Burkard, in *Handbook of Theoretical and Computational Nanotechnology*, edited by M. Rieth and W. Schommers (American Scientific Publishers, Stevenson Ranch, CA, 2006), Vol. 3.

[5] H.-A. Engel, L. P. Kouwenhoven, D. Loss, and C. M. Marcus, Quant. Info. Proc. **3**, 115 (2004).

[6] H. J. Krenner, S. Stufler, M. Sabathil, E. C. Clark, P. Ester, M. Bichler, G. Abstreiter, J. J. Finley, and A. Zrenner, New J. Phys. **7**, 184 (2005).

[7] J. M. Taylor, H.-A. Engel, W. Dür, A. Yacoby C. M. Marcus, P. Zoller, and M. D. Lukin, Nat. Phys. **1**, 177 (2005).

[8] S. Foletti, H. Bluhm, D. Mahalu, V. Umansky, and A. Yacoby, Nat. Phys. **5**, 903 (2009).

[9] E. A. Laird, J. M. Taylor, D. P. DiVincenzo, C. M. Marcus, M. P. Hanson, and A. C. Gossard, Phys. Rev. B **82**, 075403 (2010).

[10] A. Ghosal, A. D. Guclu, C. J. Umrigar, D. Ullmo, and H. U. Baranger, Phys. Rev. B **76**, 085341 (2007).

[11] A. Ghosal, A. D. Guclu, C. J. Umrigar, D. Ullmo, and H. U. Baranger, Nat. Phys. **2**, 336 (2006).

[12] D. Loss and D. P. DiVincenzo, Phys. Rev. A **57**, 120 (1998).

[13] G. Burkard, D. Loss, and D. P. DiVincenzo, Phys. Rev. B **59**, 2070 (1999).

[14] R. Hanson, L. P. Kouwenhoven, J. R. Petta, S Tarucha, and L. M. K. Vandersypen, Rev. Mod. Phys. **79**, 1217 (2007).

[15] A. J. Ramsay, Semicond. Sci. Technol. **25**, 103001 (2010).

[16] D. V. Averin and V. J. Goldman, Solid State Commun. **121**, 25 (2001).

[17] A. Y. Kitaev, Ann. Phys. **303**, 2 (2003).

[18] S. Das Sarma, M. Freedman, and C. Nayak, Phys. Rev. Lett. **94**, 166802 (2005).

[19] H. Bombin and M. A. Martin-Delgado, Phys. Rev. Lett. **98**, 160502 (2007).

[20] D. P. DiVincenzo, Fortschr. Phys. **48**, 771 (2000).

[21] L.-M. Duan, E. Demler, and M. D. Lukin, Phys. Rev. Lett. **91**, 090402 (2003).

[22] A. Bertoni, M. Rontani, G. Goldoni, and E. Molinari, Phys. Rev. Lett. **95**, 066806 (2005).

[23] J. I. Climente, A. Bertoni, M. Rontani, G. Goldoni, and E. Molinari, Phys. Rev. B **74**, 125303 (2006).

[24] J. I. Climente, A. Bertoni, G. Goldoni, M. Rontani, and E. Molinari, Phys. Rev. B **76**, 085305 (2007).

[25] M. Governale, Phys. Rev. Lett. **89**, 206802 (2002).

[26] N. Kumada, K. Muraki, and Y. Hirayama, Science **313**, 329 (2006).

[27] Y. Nishi, P. A. Maksym, D. G. Austing, T. Hatano, L. P. Kouwenhoven, H. Aoki, and S. Tarucha, Phys. Rev. B **74**, 033306 (2006).

[28] M. Ciorga, M. Korkusinski, M. Pioro-Ladriere, P. Zawadzki, P. Hawrylak, and A. S. Sachrajda, Phys. Status Solidi **238**, 325 (2003).

[29] A. S. Sachrajda, M. Korkusinski, P. Hawrylak, M. Ciorga, M. Pioro-Ladriere, and P. Zawadzki, J. Magn. Magn. Mater. **272**, E1273 (2004).

[30] P. Khandelwal, A. E. Dementyev, N. N. Kuzma, S. E. Barrett, L. N. Pfeiffer, and K. W. West, Phys. Rev. Lett. **86**, 5353 (2001).

[31] G. Gervais, H. L. Stormer, D. C. Tsui, P. L. Kuhns, W. G. Moulton, A. P. Reyes, L. N. Pfeiffer, K. W. Baldwin, and K. W. West, Phys. Rev. Lett. **94**, 196803 (2005).

[32] D. Hsieh, Y. Xia, L. Wray, D. Qian, A. Pal, J. H. Dil, J. Osterwalder, F. Meier, G. Bihlmayer, C. L. Kane, Y. S. Hor, R. J. Cava, and M. Z. Hasan, Science **323**, 919 (2009).

[33] S. Mühlbauer, B. Binz, F. Jonietz, C. Pfleiderer, A. Rosch, A. Neubauer, R. Georgii, and P. Böni, Science **323**, 915 (2009).

[34] H. Saarikoski, A. Harju, M. J. Puska, and R. M. Nieminen, Phys. Rev. Lett. **93**, 116802 (2004).

[35] M. B. Tavernier, E. Anisimovas, and F. M. Peeters Phys. Rev. B **70**, 155321 (2004).

[36] H. Saarikoski and A. Harju, Phys. Rev. Lett. **94**, 246803 (2005).

[37] N. Yang, J. L. Zhu, Z. Dai, and Y. Wang, e-print arXiv:cond-mat/0701766v1 (2007).

[38] E Anisimovas, M. B. Tavernier, and F. M. Peeters, Phys. Rev. B **77**, 045327 (2008).

[39] S.-R. Eric Yang, N. Y. Hwang, and S. Park, Phys. Rev. B **72**, 165337 (2005).

[40] A. Petkovic and M. V. Milovanovic, Phys. Rev. Lett. **98**, 066808 (2007).

[41] M. V. Milovanovic, E. Dobardzic, and Z. Radovic, Phys. Rev. B **80**, 125305 (2009).

[42] K. Moon, H. Mori, K. Yang, S. M. Girvin, A. H. MacDonald, L. Zheng, D. Yoshioka, and S. C. Zhang, Phys. Rev. B **51**, 5138 (1995).

[43] L. Jacak, P. Hawrylak, and A. Wójs, *Quantum Dots* (Springer, Berlin, 1997).

[44] These orbital wave functions are well known. However, various errors in sign and factors exist in several published versions. The expression shown in Eq. (4) is correct both in terms of the energy eigenvalue and, importantly, in terms of relations such as $a^{\dagger}|n,m) = \sqrt{n+1}|n+1,m)$.

[45] M. Abramowitz and I. A. Stegun, *Handbook of Mathematical Functions: With Formulas, Graphs, and Mathematical Tables* (Dover, New York, 1965).

[46] J. Kyriakidis, M. Pioro-Ladriere, M. Ciorga, A. S. Sachrajda, and P. Hawrylak, Phys. Rev. B **66**, 035320 (2002).

[47] C. J. Stevenson and J. Kyriakidis, Can. J. Phys. **89**, 213 (2011).

[48] H. Saarikoski, S. M. Reimann, A. Harju, and M. Manninen, Rev. Mod. Phys. **82**, 2785 (2010).

[49] H.-B. Braun and D. Loss, Phys. Rev. B **53**, 3237 (1996).

[50] C. J. Stevenson and J. Kyriakidis (unpublished).

[51] R. Hanson, L. H. Willems van Beveren, I. T. Vink, J. M. Elzerman, W. J. M. Naber, F. H. L. Koppens, L. P. Kouwenhoven, and L. M. K. Vandersypen, Phys. Rev. Lett. **94**, 196802 (2005).

[52] C. Barthel, D. J. Reilly, C. M. Marcus, M. P. Hanson, and A. C. Gossard, Phys. Rev. Lett. **103**, 160503 (2009).

[53] J. W. Negele and H. Orland, *Quantum Many-particle Systems* (Addison-Wesley, Reading, MA, 1988).